Phase transitions of titanite $CaTiSiO_5$ from density functional perturbation theory

Thomas Malcherek[1] and Michael Fischer[2,3]
[1]*Mineralogisch-Petrographisches Institut, Universität Hamburg, Grindelallee 48, 20146 Hamburg, Germany*
[2]*Fachgebiet Kristallographie, Fachbereich Geowissenschaften, Universität Bremen, Klagenfurter Straße 2-4, 28359 Bremen, Germany*
[3]*MAPEX Center for Materials and Processes, Universität Bremen, 28359 Bremen, Germany*

(Received 5 July 2017; revised manuscript received 13 December 2017; published 14 February 2018)

Phonon dispersion of titanite $CaTiSiO_5$ has been calculated using the variational density functional perturbation theory. The experimentally known out-of-center distortion of the Ti atom is confirmed. The distortion is associated with a B_u mode that is unstable for wave vectors normal to the octahedral chain direction of the $C2/c$ aristotype structure. The layer of wave vectors with imaginary mode frequencies also comprises the Brillouin zone boundary point Y (0,1,0), which is critical for the transition to the $P2_1/c$ ground-state structure. The phonon branch equivalent to the imaginary branch of the titanite aristotype is found to be stable in malayaite $CaSnSiO_5$. The unstable phonon mode in titanite leads to the formation of *trans*oriented short and long Ti-O1 bonds. The Ti as well as the connecting O1 atom exhibit strongly anomalous Born effective charges along the octahedral chain direction [001], indicative of the strong covalency in this direction. Accordingly and in contrast to malayaite, LO-TO splitting is very large in titanite. In the $C2/c$ phase of titanite, the Ti-O1-Ti distortion chain is disordered with respect to neighboring distortion chains, as all chain configurations are equally unstable along the phonon branch. This result is in agreement with diffuse x-ray scattering in layers normal to the chain direction that is observed at temperatures close to the $P2_1/c$ to $C2/c$ transition temperature and above. The resulting dynamic chains of correlated Ti displacements are expected to order in two dimensions to yield the $P2_1/c$ ground-state structure of titanite.

DOI: 10.1103/PhysRevMaterials.2.023602

I. INTRODUCTION

Early transition-metal cations with a d^0 electron configuration, e.g., $M = Ti^{4+}$, Nb^{5+}, constitute a crucial ingredient of oxide ferroelectrics [1]. These materials are commonly built of corner-sharing MO_6 octahedra, with the M cation displaced off center due to the hybridization of the empty d^0 states of the transition metal M with filled $2p$ states of the oxygen ligands [2,3]. Depending on the connectivity of the octahedral framework, chainlike dynamic correlations of the M-cation displacements may occur in the paraeletric state, causing characteristic diffuse scattering effects [4–7]. Freezing of such linear correlations then governs the symmetry changes and the formation of the distorted phases on lowering the temperature. In the cubic perovskites $BaTiO_3$ and $KNbO_3$ the chain correlations occur along all ⟨100⟩ directions in the paraelectric state [4,7,8]. Compounds with lower-dimensional connectivity of the MO_6 octahedra might reduce the occurrence of similar chain correlations to one or two dimensions. This is the case in the mineral titanite $CaTiSiO_5$.

Titanite occurs as an accessory mineral in a wide variety of magmatic and metamorphic rocks. Natural titanite crystals are often contaminated with significant amounts of Fe, Al, Nb, Ta, rare-earth elements, and other impurities. Synthetic, Zr-doped titanite has recently been suggested as a high-temperature capacitor ceramic material [9]. Parallel, kinked chains of transcorner sharing and distorted MO_6 octahedra constitute titanite's characteristic structural element. For the structure setting used in the following, parallel chains extend along the [001] direction.[1] The octahedral chains are separated by isolated SiO_4 tetrahedra. Voids between the octahedral chains and the connecting tetrahedra are filled by the Ca cations (Fig. 1). In the ground-state structure of $CaTiSiO_5$, space-group symmetry $P2_1/c$, the Ti atoms are cooperatively displaced towards the corner-sharing oxygen atom O1. The displacement is antipolar, i.e., uniform within individual chains of octahedra, but antiparallel with respect to nearest-neighbor chains (Fig. 2). At approximately 487 K, titanite transforms to a high-temperature structure with space-group symmetry $C2/c$ [10–12]. Here, Ti nominally occupies the center of its oxygen coordination environment. However, diffuse x-ray scattering in planes normal to [001] indicates that correlated displacements persist along the [001] direction in the high-temperature phase [13,14]. At 825 K, another transition has been observed [15–19]. It has been inferred [20] that the $C2/c$ titanite structure observed at pressures above 3.5 GPa [21] is similar to the crystal structure above 825 K. Starting from the high-temperature phase, diffuse scattering intensifies in lens-shaped maxima around the $h + k =$ odd reciprocal lattice points, eventually culminating in sharp diffraction maxima that mark the transition to the $P2_1/c$ phase [14] and accompanying

[1]All crystallographic directions and space-group symmetries are given in reference to standard setting (unique axis b, cell choice 1) in this work [23] and experimental data from the literature have been transformed to this standard setting when necessary.

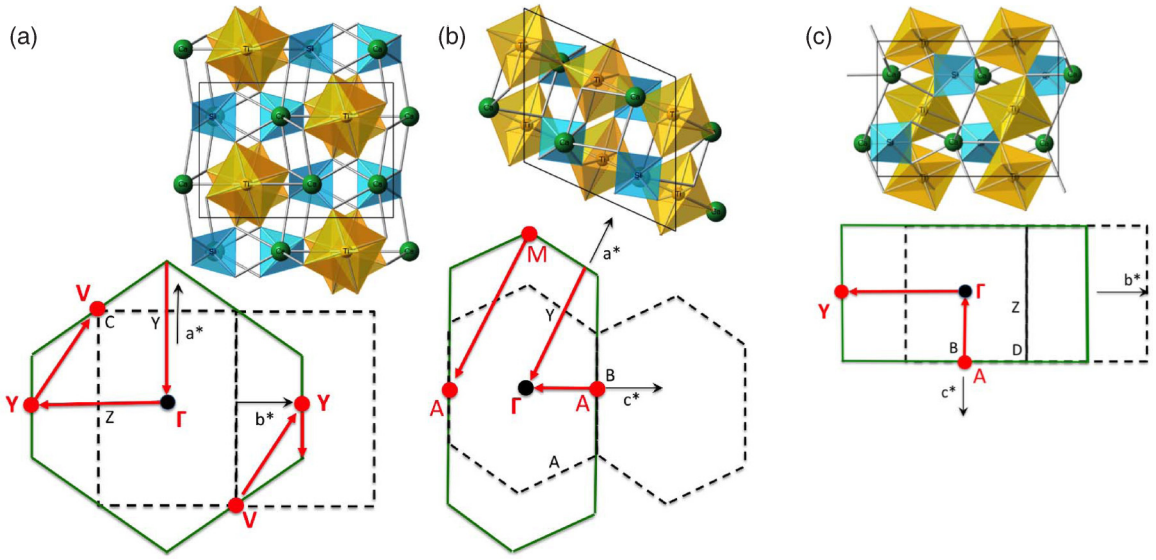

FIG. 1. The titanite crystal structure in projection along [001] (a), along [010] (b), and along [100] (c). TiO_6 octahedra are shown in yellow, SiO_4 tetrahedra in blue, and Ca atoms in green color. The outline of the first BZ for the $C2/c$ aristotype (solid green lines) and for the monoclinic P lattice (broken lines) is given for all orientations. Red lines and symbols indicate sections of the calculated phonon dispersion path in the aristotype structure. Smaller black symbols indicate special points of the $P2_1/c$ BZ.

static displacement of mainly the Ti and Ca atoms. Correlated Ti displacements along the octahedral chain direction have been used to model this diffuse scattering intensity [14] (Fig. 2). Cylindrically elongated antiphase domains parallel [001] confirm the tendency to accumulate faults in the displacement ordering normal to the chain direction. The domains become dynamic close to the phase transition temperature and the domain elongation increases with increasing cycling through the phase transition temperature [13]. Similarly elongated antiphase domains have been observed in the Ge analog compound of titanite [22], $CaTiGeO_5$. The stability of the distorted $P2_1/c$ polymorph over the $C2/c$ aristotype structure is controlled by the nature of the metal cation replacing Ti in titanite [23]. If Ti is substituted by increasing amounts of Sn [24], the ordered $P2_1/c$ phase is quickly destabilized. A rapid drop of the critical temperature and eventual disappearance of the structural distortion at room temperature has also been observed for the substitution of Zr for Ti in $Ca(Ti,Zr)GeO_5$ solid solutions [25] and in other titanite ceramics [9].

Similarities between the structural distortions and phase transitions occurring in titanite with those of the oxide ferroelectrics of the perovskite structure type have been noted early on [10]. Chain correlations similar to those observed in the titanite compounds are known to occur in the perovskite structured compounds $BaTiO_3$ [7], $KNbO_3$ [4,6], and also in the pyrochlore $Cd_2Nb_2O_7$ [26]. Here, we report linear response density functional theory (DFT) calculations that confirm the instability of dynamic linear displacement chains in titanite, as indicated by imaginary frequencies of optical phonons in layers of reciprocal space normal to the [001] direction. We first discuss the computed average crystal structure of titanite and compare it to experimental data. Then, we present the phonon dispersion in the ground-state structure and compare it to previous computations and available spectroscopic data. Finally, the results of the phonon dispersion calculation in the aristotype structure are discussed in the context of correlated cation displacements, verifying the occurrence of two-dimensionally arranged linear displacement correlations as the driving force behind the phase transition to the antipolar ground-state structure of titanite.

II. METHODOLOGY

First-principle calculations were performed by means of variational density functional perturbation theory [27,28] as implemented in the CASTEP computer code [29,30]. The plane-wave basis-set cutoff was set to 1000 eV. Norm-conserving pseudopotentials from the Bennett and Rappe pseudopotential library [31], generated using the OPIUM code [32], have been employed. An irreducible set of 16 and 5 k points in the Brillouin zone (BZ) has been sampled for the $C2/c$ and $P2_1/c$ calculations, respectively. The Monkhorst-Pack mesh was $4 \times 4 \times 3$ and $3 \times 2 \times 3$, respectively. Force convergence with respect to the size of these meshes has been verified. Phonon calculations were conducted with the zero-pressure optimized crystal structure. Calculations for the base-centered lattice were carried out in a primitive setting with transformed lattice parameters $a = b \neq c, \alpha = \beta \neq \gamma$. A $2 \times 2 \times 2\,k$-mesh size was used to calculate the phonon dispersion in the $C2/c$ symmetry. Tests using a $4 \times 4 \times 3\,k$ mesh did not yield significantly different phonon dispersion. The exchange-correlation (XC) energy contributions have been treated in the generalized gradient approximation (GGA) developed by Perdew, Burke, and Ernzerhof (PBE) [33], the revised PBE (RPBE) scheme [34], and PBE for solids (PBEsol) [35]. The only difference between the PBE and RPBE XC approximations resides in the functional form of the exchange enhancement

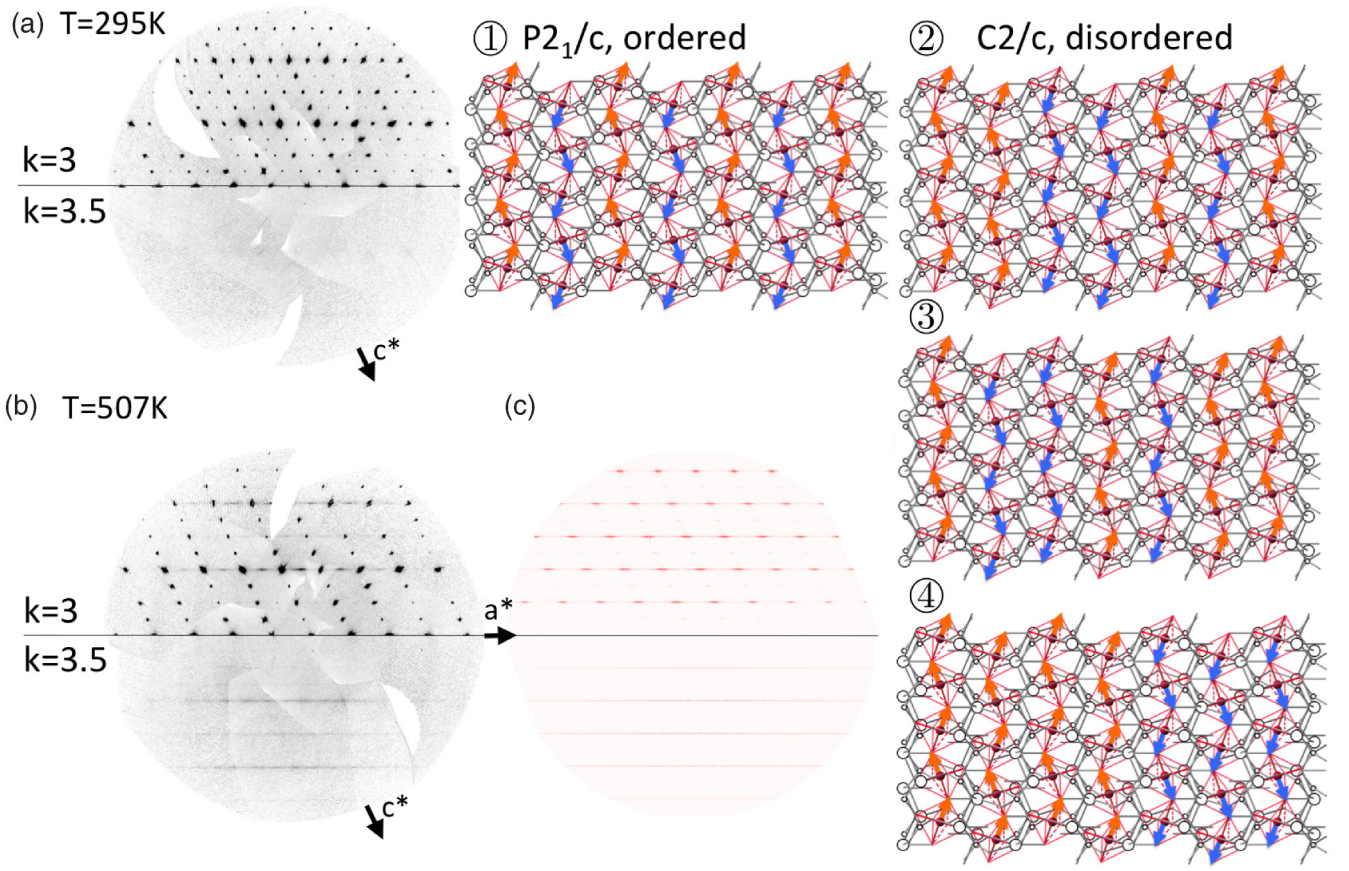

FIG. 2. Order-disorder model of the $P2_1/c$–$C2/c$ phase transition in titanite. The ordered configuration (1) is realized in the low-temperature $P2_1/c$ crystal structure. Ti off-center displacements are indicated by arrows. (a) Reconstructed x-ray diffraction intensity in the $h3l$ (upper half) and $h3.5l$ (lower half) layers of reciprocal space only shows sharp Bragg diffraction maxima at $T = 295\ \mathrm{K} \ll T_c$. (b) At $T = 507\ \mathrm{K} > T_c$ sharp superstructure diffraction maxima are replaced by diffuse scattering, broadened in layers normal to [001] (*in situ* heated synthetic titanite single crystal [47] measured using a Nonius KappaCCD x-ray diffractometer with $\lambda = 0.7107$ Å). (c) Diffuse scattering modeled based on linearly correlated Ti displacements with lateral disorder. Schematic example configurations are shown in (2), (3), and (4). Actual configurations of the model are chosen by importance sampling based on a two-dimensional Ising model, with the displacement direction of each chain (blue and orange arrows) mapped to individual spins [14].

factor $F_x(s)$, that rises more rapidly with the reduced density gradient $s = |\nabla\rho|/[2(3\pi^2)^{1/3}\rho^{4/3}]$ in RPBE compared to PBE [34,36]. $F_x(s)$ approaches the same value 1.804 for large s in both approximations. GGA functionals commonly tend to overestimate lattice parameters, corresponding to a negative pressure difference. This error is systematically larger in RPBE, caused by the steeper increase of $F_x(s)$ relative to the PBE functional. Conversely, RPBE on average yields more accurate cohesive energies than PBE, due to the same steepness in $F_x(s)$. The reason to consider different GGA approximations was that, while testing structural relaxation using various XC functionals, it became clear that several of them did either not reproduce the distorted ground-state structure of titanite or underestimated the degree of structural distortion considerably. This is the case with the PBEsol functional [35] in particular, which invokes a slowly increasing form of $F_x(s)$ and is known to calculate accurate lattice parameters [36,37]. To the authors knowledge, only few examples of phonon dispersion calculations based on the RPBE functional exist in the literature [38].

III. RESULTS AND DISCUSSION

A. Average crystal structure

Optimized lattice parameters are shown in Table I. The calculated lattice parameters show positive volume strain of about 4% (PBE) and 7% (RPBE) in comparison to cell parameters measured at room temperature [16]. The smallest positive deviation (0.9%) is obtained with the PBEsol functional. The positive volume strain is expected for PBE-type XC functionals. In order to compare with experimental data pertaining to the phase transition in titanite, the excess volume can be eliminated by calculating the spontaneous strain resulting from the $P2_1/c$ lattice parameters with the calculated $C2/c$ parameters as reference. The resulting strain parameters are shown in the lower part of Table I in comparison to experimental room-temperature strain data [16]. At zero temperature, larger, saturated strain components than at room temperature are expected. Therefore, the larger calculated values in Table I are not entirely unreasonable. Strain components calculated using the RPBE functional are a factor

TABLE I. Optimized lattice parameters and calculated strain components of titanite.

Space group	XC	a	b	c (Å)	β(°)	V (Å^3)
Titanite						
$P2_1/c$	PBE	6.6725	8.7961	7.1936	114.176	385.176
$P2_1/c$	RPBE	6.7523	8.8425	7.3115	114.495	397.255
$P2_1/c$	PBEsol	6.5911	8.7346	7.0898	113.856	373.293
$T = 293$ K (Ref. [16])		6.5630(5)	8.7194(8)	7.0650(6)	113.817(1)	369.86(5)
$C2/c$	PBE	6.6765	8.7982	7.1597	114.051	384.055
$C2/c$	RPBE	6.7629	8.8495	7.2289	114.250	394.459
$C2/c$	PBEsol	6.5916	8.7347	7.0846	113.835	373.113
	XC	e_{11}	e_{22}	e_{33}	e_{13}	e_V
$T = 293$ K (Ref. [16])		−0.0001	0	0.0018	−0.0006	0.0021
	PBE	−0.0006	−0.0002	0.0037	−0.0023	0.0029
	RPBE	−0.0016	−0.0008	0.0095	−0.0051	0.0071
	PBEsol	−0.0001	0.0	0.0006	−0.0004	0.0005

of 2 larger than those calculated using PBE. In comparison to experimental strain data, the calculated strain components maintain the correct sign and confirm that e_{33} is the largest component. It is remarkable that with the PBEsol functional hardly any spontaneous strain is obtained in the $P2_1/c$ phase. The calculated energy differences between the $C2/c$ and the $P2_1/c$ phases are −0.3772 kJ/mol (PBE), −1.5767 kJ/mol (RPBE), and −0.0006 kJ/mol pfu (PBEsol), matching the sequence of obtained strain parameters.

The optimized atomic coordinates of both titanite phases are shown in Table II. After appropriate transformation, the results of a previous structure relaxation [39] are in good agreement with the data for the $P2_1/c$ phase, with Ti showing the largest relative atomic shift between the two calculations (0.011 Å, mainly directed parallel [001]). The primary distortion of the low-symmetry phase with respect to the $C2/c$ parent structure is described by the Y_{2-} irrep, accompanied by an origin shift of $\frac{1}{4}$, $\frac{1}{4}$, 0 (Ref. [23]). The respective mode amplitudes and absolute atomic displacements in Å have been calculated using the AMPLIMODES program [40] with the relaxed structural parameters obtained with CASTEP. These values are compared to the mode amplitudes obtained with the structural parameters measured [15] at 100 and 530 K in Table III.

As the mode amplitudes in Table III demonstrate, PBE slightly underestimates the structural distortion, while RPBE appears to exaggerate it. This agrees with the much larger energy difference obtained using the RPBE functional. Calculations with the PBEsol functional appear to severely underestimate the structural distortion of the $P2_1/c$ phase. This agrees with the absence of spontaneous strain and with the negligible energy difference between both titanite symmetries that is obtained with this XC functional.

The structural distortion can be divided into a smaller, fully symmetric distortion Γ_{1+} that preserves the $C2/c$ parent symmetry and the larger Y_{2-} distortion that breaks the parent symmetry. The distortion can also be analyzed using the Abrahams-Kurtz-Jamieson–type relation given in Ref. [23]. This amounts to an empirical relation of $T_c = C_{AKJ}|x_M|^2$,

TABLE II. Optimized structural parameters of titanite in space group $P2_1/c$ and $C2/c$.

Position	PBE			RPBE			PBEsol		
	x	y	z	x	y	z	x	y	z
$P2_1/c$									
Ti	0.24907	0.24569	0.01191	0.24899	0.24336	0.01647	0.24953	0.24826	0.00498
Ca	0.75064	0.08023	0.74026	0.75194	0.08089	0.73352	0.75010	0.08039	0.74618
Si	0.74893	0.06901	0.2486	0.74862	0.06884	0.24895	0.74948	0.06869	0.24922
O1	0.25001	0.17773	0.2498	0.24922	0.1775	0.2475	0.25026	0.17725	0.25049
O2	0.93311	0.18624	0.40645	0.93274	0.18640	0.40223	0.93363	0.18612	0.41146
O3	0.56426	0.31412	0.59083	0.56333	0.31483	0.59447	0.56525	0.31393	0.58718
O4	0.14862	0.03639	0.88161	0.15085	0.03659	0.87916	0.14572	0.03723	0.88248
O5	0.35086	0.46325	0.11888	0.34784	0.46372	0.11851	0.35412	0.46248	0.11821
$C2/c$									
Ti	0	0	0	0	0	0	0	0	0
Ca	0	0.32916	1/4	0	0.32826	1/4	0	0.33024	1/4
Si	0	0.68031	1/4	0	0.67946	1/4	0	0.68121	1/4
O1	0	0.07109	1/4	0	0.06954	1/4	0	0.07259	1/4
O2	0.68440	0.06347	0.40794	0.68484	0.06293	0.40396	0.68417	0.06384	0.41218
O3	0.60045	0.28593	0.11747	0.59657	0.28472	0.11659	0.60412	0.28730	0.11771

TABLE III. Normalized mode amplitudes, referred to the primitive parent cell, and absolute atomic displacements. Experimental results in the final column are based on the crystal structures measured at 100 and at 530 K as reported in Ref. [15].

Irrep.	Isotr. Subgroup	Amplitude (Å)			
		PBE	RPBE	PBEsol	Expt.
Γ_{1+}	$C2/c$	0.030	0.078	0.006	0.032
Y_{2-}	$P2_1/c$	0.171	0.264	0.098	0.191
Atomic displacement (in Å)					
Δ_{Ti}		0.096	0.137	0.04	0.115
Δ_{Ca}		0.073	0.129	0.027	0.067
Δ_{Si}		0.011	0.018	0.005	0.013
Δ_{O1}		0.011	0.031	0.004	0.005
Δ_{O21}		0.011	0.016	0.005	0.009
Δ_{O22}		0.011	0.021	0.005	0.019
Δ_{O31}		0.008	0.033	0.002	0.012
Δ_{O32}		0.012	0.019	0.004	0.010

where $|x_M|$ is the absolute, static M-cation displacement (in Å) and $C_{AKJ} = 38\,404$ K Å^{-2}. Using this relation, the Ti displacements obtained by DFT structure optimization can be converted to $P2_1/c \leftrightarrow C2/c$ transition temperatures of 353 K (PBE) and 710 K (RPBE). These values are below and above the experimental transition temperature of 487 K, respectively. Starting from the much smaller distortion obtained with the PBEsol functional, T_c would amount to just 61 K. Altogether, there are strong indications that the PBEsol functional does not perform very well with regard to describing the properties of the distorted titanite ground-state structure and we will concentrate on the PBE and RPBE functionals in the following.

Figure 2 summarizes the effects of the phase transition as observed by x-ray diffraction. At temperatures above T_c, Bragg diffraction maxima with $h + k =$ odd vanish. These positions correspond to the special position Y at the $C2/c$ BZ boundary (Fig. 1). Note that the BZ boundary area close to this point directly borders on the next BZ along the $\mathbf{b}^\star$ direction. The Bragg diffraction maxima are replaced by diffuse scattering (DS) maxima above T_c. These DS maxima are sharp in [001] direction (the vertical direction in Fig. 2) and very broad normal to it. The resulting diffuse scattering sets in at temperatures far below T_c, but is very weak at room temperature (cf. Fig. 2). It extends in sheets normal to [001], as can be seen in the $h3.5l$ layer. High diffuse scattering intensity is observed for even values of l, whereas sheets with $l =$ odd are weak to absent. This DS and its temperature dependence can be approximated using fully Ti-displaced chains of TiO_6 octahedra, that can flip their sense of distortion according to the spin values of a two-dimensional antiferromagnetic Ising-model [14]. Results of the model calculations (red color) are given next to the 507-K diffraction images in Fig. 2(c). Fourier transformation has been conducted using the DISCUS program [41] and averaged over 25 model configurations. Details of the model are described in Ref. [14].

B. Phonon dispersion in the titanite ground-state structure

The calculated phonon dispersion curves for the distorted crystal structure in space group (SG) $P2_1/c$ are shown in Fig. 3. Some of the special points [42] along the chosen path B-Γ-Z-C-Y-A-E-D belong to the BZ sections shown in Fig. 1 (small black symbols). The path sections between Z and C as well as between A and D follow the boundary of the BZ and are marked by degenerate frequencies. In terms of calculated frequencies, the results are similar to those given in Ref. [39] (B-Γ-Z-C-Y). There are 96 modes in SG $P2_1/c$. Of the 93 optic modes, 48 are Raman active (24 A_g + 24 B_g) and 45 are infrared active (23 A_u + 22 B_u). The phonon branches are narrowly spaced in the range up to 550 cm^{-1}. These modes involve movements of all atoms. The lowest-frequency modes are dominated by Ca motion parallel to [001]. There is a gap

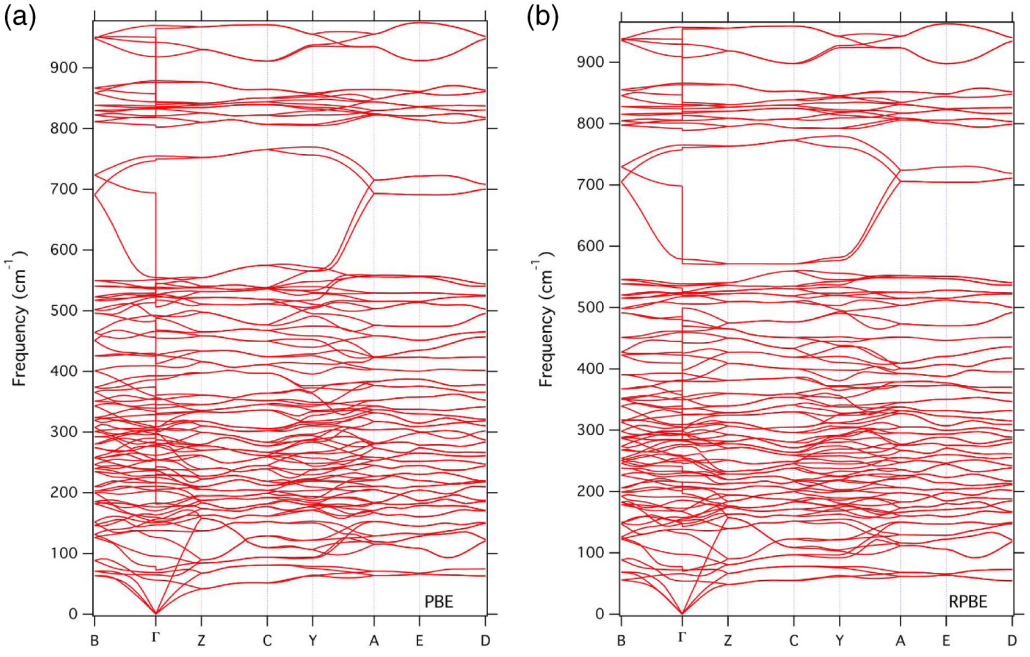

FIG. 3. Phonon dispersion curves for the $P2_1/c$ phase calculated using the PBE (a) and the RPBE (b) XC functionals.

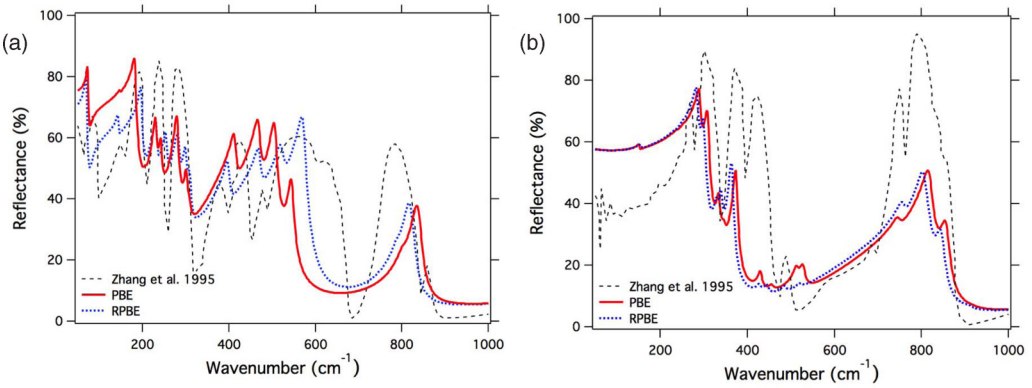

FIG. 4. Calculated infrared reflectance spectra. Black, dashed curves indicate the corresponding polarized single-crystal reflectance measurements published in Ref. [12], with electric field vector parallel to the chain direction (a) and parallel to $\mathbf{b}^\star$ (b).

in the phonon density between 550 and 800 cm^{-1}. The region above the gap is dominated by Si-O stretching vibrations. In the RPBE calculation, the four phonon branches within the gap are clearly separated from the region above and below it. In the RPBE case, a clear correspondence exists between the LO and TO branches of the B_u mode close to 700 cm^{-1} inside this gap. Contrary to this, it is rather difficult to identify a single transverse optical (TO) mode that corresponds to the longitudinal optical (LO) branch of the B_u mode at 694 cm^{-1} in the PBE case. While the mode is dominated by uniform O1 motion parallel [001], with weaker Ti motion directed opposite to this, such a vibrational pattern is not clearly identifiable for any phonon mode with frequency below 700 cm^{-1} in the PBE calculation. Agreement of the LO mode eigenvectors is best with the TO mode at 506.2 cm^{-1} though. It should be noted that there is no exact one-to-one correspondence between the LO and TO sides of the branch for large LO-TO splittings and multiple TO modes can contribute to the formation of an individual LO mode [43].

In Figs. 4(a) and 4(b), the calculated IR reflectance is compared to published infrared reflectance measurements [12] of a synthetic titanite single crystal. Figure 4(a) shows the calculated reflectance in [001] polarization. The electric field vector was parallel to [100] in the setting chosen in Ref. [12], which corresponds to [001] in the standard setting of the $P2_1/c$ titanite structure used here. In the PBE approximation, the intense TO mode at 506 cm^{-1} appears at the bottom of the [001]-polarized, broad signal centered at 570 cm^{-1}, while it appears as a stronger signal in the middle of this region in the RPBE approximation. With both XC functionals, the calculated LO frequency corresponds very well to the sharp reflectivity minimum observed close to 700 cm^{-1}. Figure 4(b) shows the observed and calculated reflectance in polarization parallel to $\mathbf{b}^\star$, where the band at 570 cm^{-1} is absent, both in the calculated and in the observed spectra. Calculated reflectance curves have been obtained from the imaginary part of the dielectric permittivity ϵ_2 as calculated by CASTEP. The real part ϵ_1 of the dielectric permittivity was obtained by Kramers-Kronig transformation. The refractive index is $n = [\epsilon_1 + (\epsilon_1^2 + \epsilon_2^2)^{1/2}]^{1/2}/2^{1/2}$ and the reflectance as shown in Fig. 4 was then obtained as $R = 100(n-1)^2/(n+1)^2$.

The calculated frequencies and intensities of Raman active modes are compared with available experimental data measured at 110 K (Ref. [17]) and at room temperature [44] in Table IV. The most intense Raman signal occurs close to 600 cm^{-1} in titanite. The A_g mode at 579 (RPBE) and at 555 cm^{-1} (PBE) can be assigned to this signal. It is dominated by O1 motion, causing coupled Ca-O1 and Ti-O1 bond stretching and libration. In accordance with experiment, this A_g mode is indeed the most intense mode of the RPBE spectrum, while a lower-frequency A_g mode has higher intensity in the PBE approximation. Very similar O1 motion is observed for the B_u mode at 693 cm^{-1}, but in this case the O1 atoms of adjacent chains move in phase, rather than antiparallel as for the A_g mode. The phonon mode that would have to soften in the $P2_1/c$ phase to eliminate the static distortion on approaching the phase transition to the aristotype structure from the low-temperature side, is indeed expected to have A_g symmetry. A mode observed at 110 cm^{-1}, corresponding to the calculated A_g mode at 95.3 cm^{-1} (PBE, Table IV), does indeed match the above requirement of resetting the Ti-atom position. However, it does not appear to soften unusually on temperature increase [17], but its scattering intensity rapidly drops between 433 and 507 K. In an order-disorder scenario with a deep double-well potential and pseudo-Ising-type behavior, as postulated in Ref. [14], the static distortion arises entirely from preferred population of one of the double wells. The Ti atom would remain close to the bottom of the potential well and no significant temperature dependence of the frequency of the restoring phonon mode would be observed in this case. Instead, a "central mode" occurs [45], due to the hopping between the available potential wells that develops in the vicinity of T_c.

C. Phonon dispersion in the titanite aristotype structure

Figures 5 and 6 show the calculated phonon dispersion curves for the $C2/c$ aristotype structure using the PBE and RPBE functionals, respectively. Of the 45 optic modes, 21 are Raman active (9 A_g + 12 B_g) and 24 are infrared active (11 A_u + 13 B_u). Imaginary frequencies with little or no dispersion occur along the entire path section Γ-Y-V-Y-Γ (Fig. 1), i.e., for wave vectors normal to [001]. These imaginary phonon frequencies are represented by negative values in Figs. 5 and 6. As Fig. 1 shows, the chosen path crosses the Y point twice along two directions (parallel to $\mathbf{b}^\star$ and parallel to $\mathbf{a}^\star$). For the corresponding propagation directions, the B_u mode constitutes a pure Ti-O1 bond stretching motion, with

TABLE IV. Comparison of calculated and observed position and intensity of Raman active modes. Experimental data at 300 and at 110 K have been obtained by fitting the spectra reported in Refs. [44] and [17], respectively.

Irrep	$\bar{\nu}_{PBE}$ (cm^{-1})	$\bar{\nu}_{RPBE}$ (cm^{-1})	I_{PBE} (%)	I_{RPBE} (%)	$\bar{\nu}_{300\,K}$	I_{Or1} (%)	I_{Or2}(%)	$\bar{\nu}_{110\,K}$	$I_{110\,K}$(%)
A_g	56.061	53.808	0.67	0.14	80	8.1	3.8	78.3	4.5
B_g	64.771	65.66	0.12	0.065					
A_g	95.317	97.493	8.4	1.2	110	0.3	0.4	109.6	3
A_g	126.62	131.99	16	1.9	144	1.9	1.9	142.5	7
B_g	137.88	138.44	0.27	0.2					
A_g	153.21	147.5	11	0.94	164	0.8	4.2	165	2.4
B_g	156.53	155.04	0.15	0.02					
A_g	159.55	168.25	5	2	179	2.2	1.8	177	9
B_g	176.72	172.75	0.28	0.08					
A_g	182.85	185.88	1.7	0.32	200	1.6	0.2	195	3.3
B_g	202.81	191.56	0.4	0.14	217	1.9	0.6		
B_g	210.61	206.9	0.09	0.08					
A_g	216.31	208.06	12	2.1	233	1.2	0.8	229	1.1
A_g	228.76	225.77	3.1	0.53	252	9.5	5.6	246	6.2
B_g	236.23	233.47	0.05	0.01					
A_g	253.96	254.81	43	8.3	258	1.1	2.3	251	8.4
B_g	261.56	257.56	0.18	0.16					
A_g	276.39	282.09	8.9	8.7	285	4.4	6.3	279	8.6
B_g	278.94	273.73	0.95	0.46					
A_g	281.46	284.63	10	2.5	285	4.4	6.3		
A_g	296.63	293.61	2	2.8	302	1.2	1.7	294	3.8
B_g	308.45	292.7	1.3	0.57					
B_g	302.85	298.79	0.09	0.09					
A_g	318.38	309.11	16	12	314	19.5	7.2	305.6	16.5
B_g	328.86	324.89	1.7	0.41	328	1.1	7	321	2.7
B_g	353.21	349.5	0.86	0.64	351	1.5	1.5	340.5	14
A_g	356.1	353.74	0.92	0.57	351	1.5	1.5	340.5	14
B_g	386.41	381.76	0.03	0.08					
A_g	392.61	379.8	20	4.7	384	0.3	0	374	4.7
B_g	409.4	392.74	0.24	0.37					
A_g	427.29	422.51	79	17	422	6	5.9	412	5.7
A_g	489.46	505.97	100	19	535	17.3	4.5	522	30.1
B_g	492.16	461.58	2.6	1.1	465	1.5	4	452.5	9.8
B_g	522.35	518.01	0.39	0.32	524	14.2	15.7	508	9.1
A_g	524.55	522.75	11	15	556	1.4	0	543	9.6
B_g	536.07	535.69	0.12	0.21					
A_g	538.5	535.68	2.2	0.92	568	0.3	5.2		
B_g	551.06	538.74	1.1	0.21					
A_g	554.62	578.79	96	100	607	100	100	594	100
B_g	754.84	765.18	3.2	1	825	7.5	9	802	18.8
A_g	817.8	800.99	0.63	0.53	855	7.8	4.1	836	19.8
B_g	821.07	804.96	6.4	2.7	855	7.8	4.1	836	19.8
A_g	832.37	817.04	8.9	4.7	870	5.3	12.6	851	9.5
B_g	834.43	824.46	1.4	0.59					
A_g	844.04	831.21	2.7	1.6	883	0.2	7.2	863	3.3
A_g	875.99	863.34	7.2	5.2	910	2.5	2.4	895	7.9
B_g	878.8	866.03	0.19	0.12					
B_g	942.02	929.37	0.99	0.27	990	1	0	972	9.3

Ti moving along the linear O1-Ti-O1 bond direction, while O1 moves in the opposite direction. The Ti movement has a larger component parallel to [001] and a smaller component parallel to [010], while the O1 atom moves along [001] only. Freezing this phonon causes the formation of long-range ordered, alternating short and long Ti-O1 bonds along the octahedral chain direction, a pattern that is characteristic of the distorted $P2_1/c$ structure. In Fig. 7 the static structural displacement generated by the frozen B_u phonon at the Y point is compared with the experimentally observed distortion [15] of titanite at 100 K for an individual chain of TiO_6 octahedra, demonstrating excellent agreement between the frozen phonon and the structural distortion obtained at low temperatures. All wave vectors normal to [001], i.e., those without a component

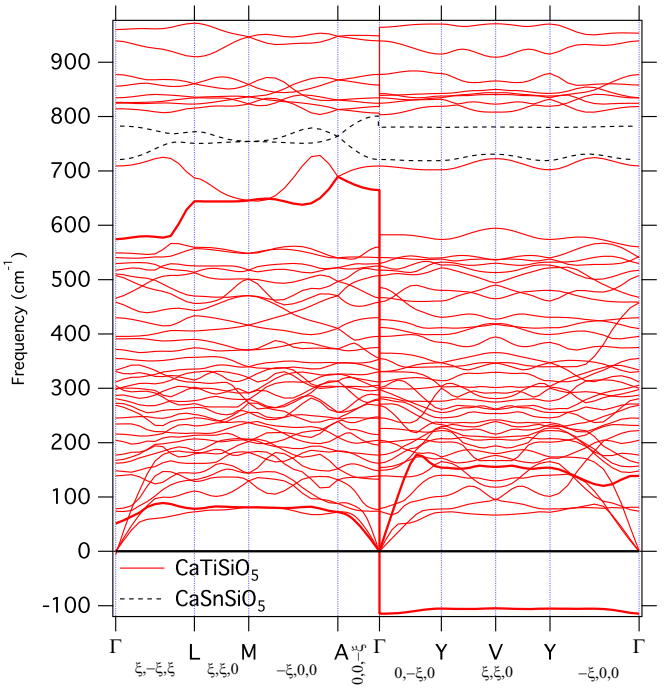

FIG. 5. Phonon dispersion curves in the $C2/c$ symmetry, calculated using the PBE XC functional. Dashed curves show two calculated phonon branches of malayaite for comparison.

in chain direction, are compatible with this kind of long-range correlated intrachain Ti-O-Ti dynamic stretching motion. A wave-vector component parallel to the chain direction would alter the correlated dynamic stretching and this type of motion

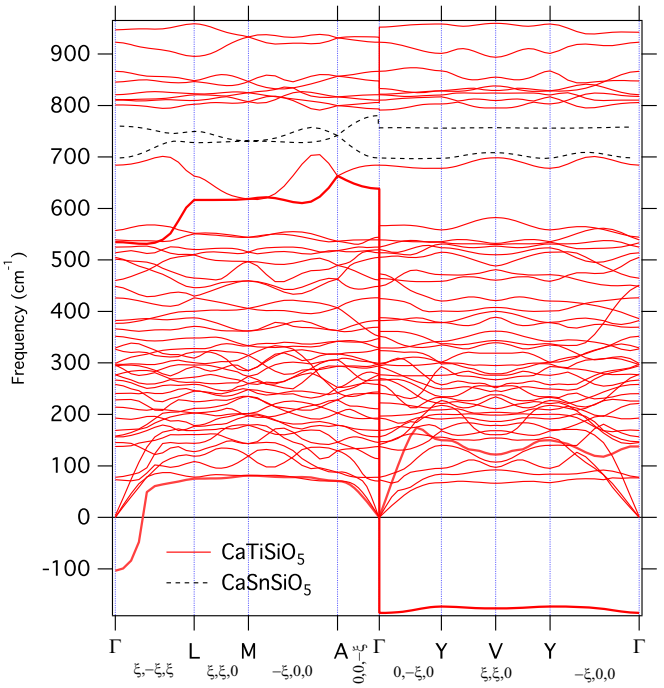

FIG. 6. Phonon dispersion curves in the $C2/c$ symmetry, calculated using the RPBE XC functional. Dashed curves show two calculated phonon branches of malayaite for comparison.

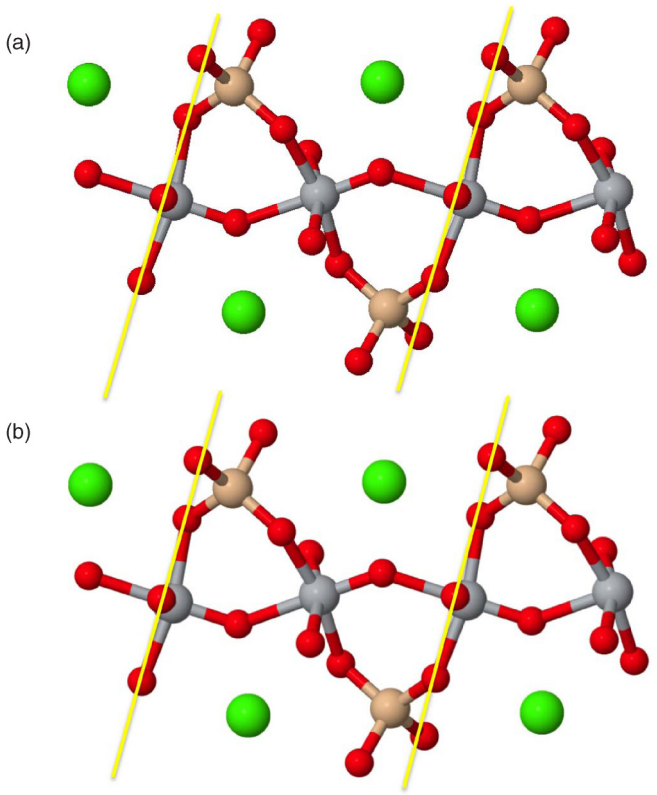

FIG. 7. A single chain of TiO_6 octahedra with bridging SiO_4 tetrahedra, (a) calculated with maximum displacement amplitude of the imaginary B_u phonon in SG $C2/c$, (b) experimentally determined at 100 K (Ref. [15]). For clarity, distortions have been exaggerated by a factor of 2 in both cases. Titanium atoms are shown in gray, calcium atoms in green, oxygen in red, and silicon in brown color. The position of zero Ti displacement is indicated by yellow lines for two of the TiO_6 octahedra.

is therefore confined to the k_x-k_y layer of the BZ. The imaginary character of the mode indicates that the Ti atom is not located at the center of its octahedral coordination environment in the $C2/c$ aristotype structure in the zero-temperature approximation. At elevated temperatures, the mode could be stabilized by increasingly anharmonic motion, which would possibly develop into a double-well potential that favors off centering of Ti. Regarding the very large LO-TO splitting at the crossover from the $0,0,\xi$ to $0,\xi,0$ approach to the Γ point (the center of Figs. 5 and 6), there is no exact correspondence between the TO side of the mode and the LO side. Components of the Ti-O1 stretching motion exhibited by the imaginary phonon can be identified in several B_u modes on approaching the Γ point along $0,0,\xi$. Opposite Ti and O1 motion strictly along [001] contributes to the mode at 665 cm^{-1} (Fig. 5), causing Ti-O1-Ti bending in addition to Ti-O1 stretching. The mode at 354 cm^{-1} causes coupled motion of the Ti-O1 bonds parallel [001], while the lower-frequency modes at 278, 133, and 77 cm^{-1} involve small antiparallel Ti displacements along [010], that can also be identified in the unstable phonon branch. That the softest TO mode correlates with the hardest LO mode is a situation very similar to the "giant LO-TO splitting" described in the ferroelectric perovskites [43].

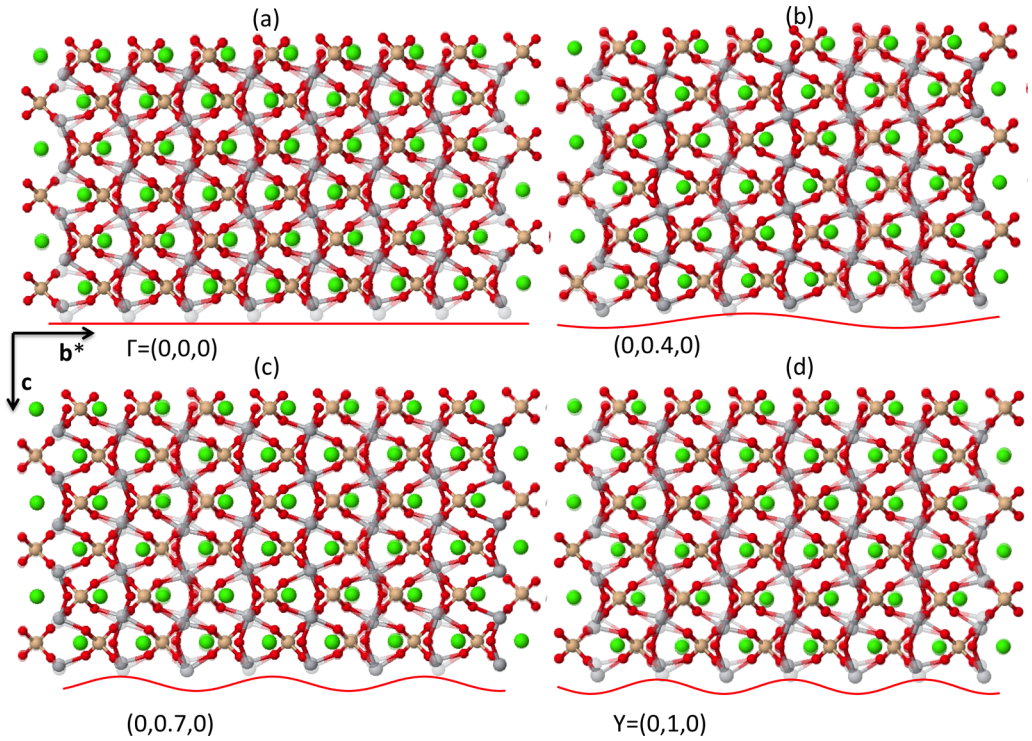

FIG. 8. Displacements caused by the imaginary frequency B_u mode in the $C2/c$ structure along the path Γ-Y, viewed in projection along $\mathbf{a}^\star$ for selected wave vectors (a)–(d). Displacements are visualized by overlays of two frozen-phonon images with opposite and exaggerated amplitudes. Red curves indicate the modulation of displacement amplitudes. Ti atoms are shown in gray, Si in brown, Ca in green, and O atoms in red color.

While the formation of the distorted $P2_1/c$ phase at the Y point (Table III) is strongly suggested by experiment and the structure is confirmed to be stable by DFT calculations, the phonon branch that causes the associated displacement has nearly constant imaginary frequency across a large part of the BZ, including but not limited to the Y point. This indicates that, at least for the effectively negative pressures induced by the PBE and RPBE functionals, the correlated atomic displacements in chain direction occur with all possible phase shifts among the parallel octahedral chains. This is pictured in Fig. 8, where two images of frozen phonons, each with maximum displacement amplitude in either positive or negative direction, are superimposed for four different points along the Γ-Y section of the BZ path. Figure 8(a) shows the potentially ferroelectric displacements at the Γ point. Here, all atoms in parallel chains move in phase. At the Y point, as the other extreme, Fig. 8(d), atoms in neighboring chains move in an antiparallel way. This frozen phonon gives rise to the formation of the ordered $P2_1/c$ structure as described above, with antipolar displacement of Ti atoms. The two intermediate wave vectors in Figs. 8(b) and 8(c) represent incommensurate modulations of the displacement amplitudes.

Interesting behavior of the phonon mode dispersion is also observed when the Γ point is approached from the L point ($\frac{1}{2}$, $\frac{1}{2}$, $\frac{1}{2}$). The mode close to 650 cm^{-1} rapidly drops to 577 cm^{-1} with no further dispersion until Γ is reached. This mode is also characterized by O1-Ti-O1 motion, causing alternating Ti-O1 bond stretching, but every second Ti does not move parallel to the chain direction, thus causing O1-Ti-O1 bond bending instead. Parallel to this, a low-frequency mode at 70 cm^{-1} starts to soften. As Γ is approached, the [001] component of the Ti movement associated with this mode increases, until, close to the BZ center, the motion of the involved atoms resembles the collective O1-Ti-O1 stretching motion observed for the imaginary frequency mode as pictured in Fig. 7. In the PBE approximation, the mode remains stable at 51 cm^{-1}, but in the RPBE approximation it is rendered imaginary as

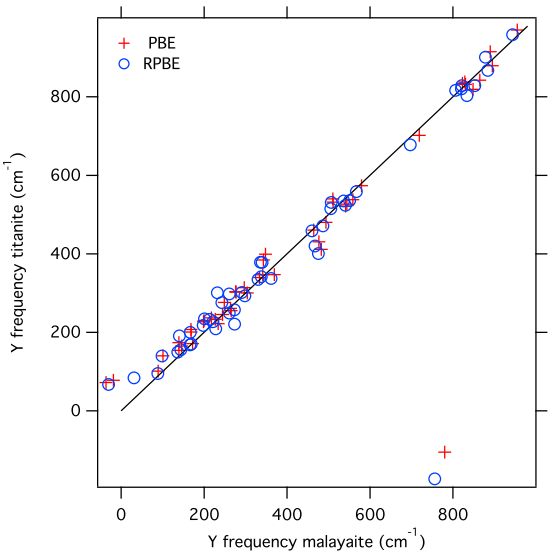

FIG. 9. Comparison of calculated mode frequencies in titanite and malayaite at the Y-zone boundary position. The line indicates equality.

TABLE V. Calculated Born effective charge tensors in the $P2_1/c$ and $C2/c$ crystal structures.

Site	PBE			RPBE		
			$P2_1/c$			
O1	−1.02150	0.00784	−0.06483	−0.98484	0.00799	−0.06902
	0.00921	−1.82193	0.32231	0.00676	−1.75020	0.43930
	−0.01666	0.14455	−6.24154	−0.00631	0.22328	−5.45165
O2	−3.54284	−0.94917	−0.21455	−3.52995	−0.97870	−0.25273
	−0.85154	−2.18325	−0.18448	−0.87823	−2.21874	−0.18949
	−0.44399	−0.09458	−1.47810	−0.49782	−0.11907	−1.43616
O3	−3.55674	−0.81115	−0.04604	−3.58179	−0.78723	−0.03132
	−0.79050	−2.11895	−0.06480	−0.79129	−2.11528	−0.03487
	−0.29093	−0.04167	−1.42562	−0.29579	−0.06088	−1.34259
O4	−1.76848	−0.14613	0.10292	−1.75625	−0.12649	0.11781
	−0.06864	−2.76100	−0.91026	−0.06267	−2.72778	−0.96718
	−0.00711	−0.86945	−2.15272	−0.01134	−0.93586	−2.16120
O5	−1.75973	−0.13210	0.07811	−1.72900	−0.10203	0.09065
	−0.05511	−2.83029	−0.74308	−0.04018	−2.83176	−0.72162
	0.03139	−0.72814	−2.08948	0.04414	−0.71006	−2.07384
Si	3.79291	0.02943	−0.39701	3.79674	0.03088	−0.41374
	−0.00168	4.24479	0.15138	−0.00836	4.25513	0.19852
	0.91673	0.02704	3.32546	0.90920	0.03164	3.34361
Ca	2.61277	−0.00324	0.04627	2.61464	0.00348	0.05057
	−0.01779	2.77223	−0.16718	−0.02815	2.79213	−0.22745
	−0.02910	0.01073	2.11588	−0.02611	0.02956	2.12307
Ti	5.24360	−0.47361	0.49512	5.17044	−0.49436	0.50779
	−0.42245	4.69839	−1.03927	−0.44040	4.59651	−0.64520
	−0.16033	0.14373	7.94612	−0.11598	0.17466	6.99877
			$C2/c$			
O1	−1.05215	0.0	−0.05729	−1.04275	0.0	−0.05900
	0.0	−1.86560	0.0	0.0	−1.83984	0.0
	−0.00512	0.0	−7.24427	0.01369	0.0	−7.37105
O2	−3.59770	0.89218	−0.12626	−3.66032	0.90984	−0.13720
	0.82572	−2.15298	0.15054	0.84758	−2.17474	0.15882
	−0.35991	0.06279	−1.50890	−0.38506	0.07984	−1.48705
O3	−1.76174	0.15271	0.08755	−1.73488	0.13946	0.10085
	0.07114	−2.82675	0.83008	0.06824	−2.84778	0.84820
	0.00725	0.79645	−2.15755	0.00902	0.81612	−2.18449
Si	3.82741	0.0	−0.41109	3.87834	0.0	−0.43293
	0.0	4.26966	0.0	0.0	4.31037	0.0
	0.93366	0.0	3.30767	0.93966	0.0	3.31231
Ca	2.60788	0.0	0.04437	2.60123	0.0	0.04937
	0.0	2.78105	0.0	0.0	2.81167	0.0
	−0.03014	0.0	2.10603	−0.02656	0.0	2.10369
Ti	5.33573	−0.48346	0.50142	5.35358	−0.52086	0.51525
	−0.41917	4.77434	−1.47836	−0.43756	4.76284	−1.45890
	−0.19307	0.13294	9.16345	−0.17471	0.14683	9.29812

well. In both cases, there is a large overlap of the eigenvectors with the imaginary phonon in the zero layer normal to [001]. This confirms that volume increase (or negative pressure), as obtained with the RPBE functional in particular, stabilizes the static distortion of the Ti atoms towards O1, as was already shown by the structure relaxation in SG $P2_1/c$. It also shows that the unstable phonon mode is stabilized for wave vectors that point away from the zero layer normal to [001], but that the correlated Ti displacement parallel to [001] quickly subsides with increasing wave-vector magnitude in this case.

The broken lines in Figs. 5 and 6 show the dispersion of two selected modes of malayaite, $CaSnSiO_5$. In malayaite the B_u mode between 700 and 800 cm^{-1}, that involves Sn and O1 motion similar to the Ti and O1 motion described above, is stable throughout the entire BZ. The LO-TO splitting is reduced to 20 cm^{-1}. The formation of the ordered $P2_1/c$ structure with corresponding short and long Sn-O bonds is indeed not observed in malayaite. All calculated mode frequencies of malayaite and titanite at the Y-zone boundary position are compared in Fig. 9, clearly indicating the outlier for the unstable titanite phonon branch that is shifted close to 800 cm^{-1} in malayaite. Most other mode frequencies do not differ by more than 50 cm^{-1}. Low-lying, Ca-dominated modes with imaginary frequencies in malayaite will be dealt with in a separate publication.

Born effective charges ($\mathbf{Z}^\star$) provide a measure for the polarization changes caused by the ionic displacements. The

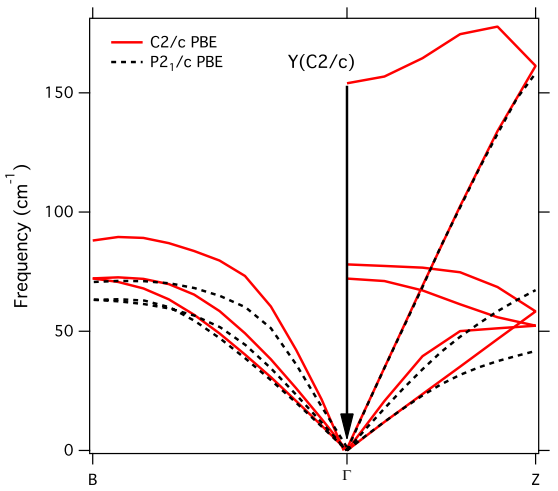

FIG. 10. Comparison of acoustic phonon branches in the $P2_1/c$ (black, dashed) and $C2/c$ (red) phases, for the path direction parallel to [010]. The arrow indicates expected softening at the zone boundary of the $C2/c$ phase.

components of $\mathbf{Z}^\star$ for the Ti and O1 atoms in the $C2/c$ aristotype structure of titanite are strongly anomalous and anisotropic (Table V). To a lesser degree, this is also the case for the ordered $P2_1/c$ phase. The deviation from the formal charge is largest for the **c** direction, with the positive charge of Ti deviating 75% from the formal charge in the $P2_1/c$ phase and more than 100% in the $C2/c$ phase. In analogy to the perovskites, the strong anomalies in the dynamic charges can be seen as indication of covalency [46] induced by hybridization of the O $2p$ electronic states with the Ti $3d$ states. These covalencies will appear along **c** on average, i.e., the average direction of Ti and O1 displacement along the Ti-O1-Ti zigzag chains that is imposed by the unstable phonon mode. The giant LO-TO splitting [43] observed for modes that involve large displacements of O1 and Ti can be related to the anomalous $\mathbf{Z}^\star$ components of these atoms. In contrast to this, $\mathbf{Z}^\star$ is much closer to the formal charges of all atoms in the $C2/c$ phase of malayaite, where no similar hybridization of the Sn and O electronic states is expected.

Figure 10 shows the acoustic mode dispersion, calculated with the PBE functional in more detail for the $0,\xi,0$ direction of approach to Γ. The dispersion of the longitudinal acoustic (LA) mode is nearly identical in both symmetries, up to the $P2_1/c$ BZ boundary at the point Z. Limited softening of the branch is observable beyond this point (folded back towards Γ in Fig. 10). The results obtained with the PBE and RPBE functionals are nearly identical close to the Γ point. As the Y-zone boundary point degenerates to a Γ point during the course of the transition to the $P2_1/c$ structure, the branches at the zone boundary have to soften considerably (indicated by the arrow in Fig. 10). Such a mode softening can be expected due to coupling with the soft phonon branch.

As is shown in Fig. 11, at the zone boundary position both transverse acoustic (TA) branches are dominated by Ca motion parallel to the octahedral chain direction. At 72.1 cm^{-1}, the Ca atoms move pairwise in opposite direction, accompanied by libration of the SiO_4 tetrahedra and sideways Ti motion, while at 78.1 cm^{-1} collinear Ca motion in chain direction dominates, with its sense alternating parallel to [010]. Static or strongly anharmonic Ti displacement within the octahedral chains, as

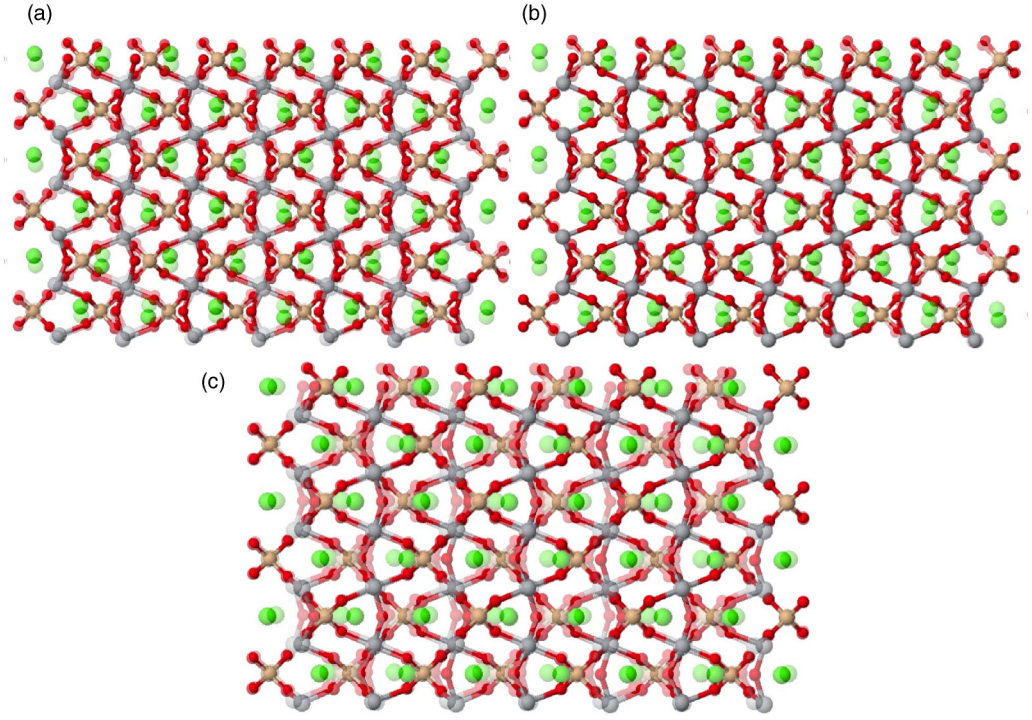

FIG. 11. Dynamic displacements associated with the three acoustic mode branches at the Y-zone boundary position, visualized by overlays of two frozen-phonon images with opposite and exaggerated amplitudes. (a) TA branches at 72.08 cm^{-1} and (b) at 78.06 cm^{-1}, (c) LA branch at 154.03 cm^{-1}. [001] runs from top to bottom, [010] from left to right. Ca atoms appear in green, Si in brown, Ti in gray, and oxygen atoms in red color.

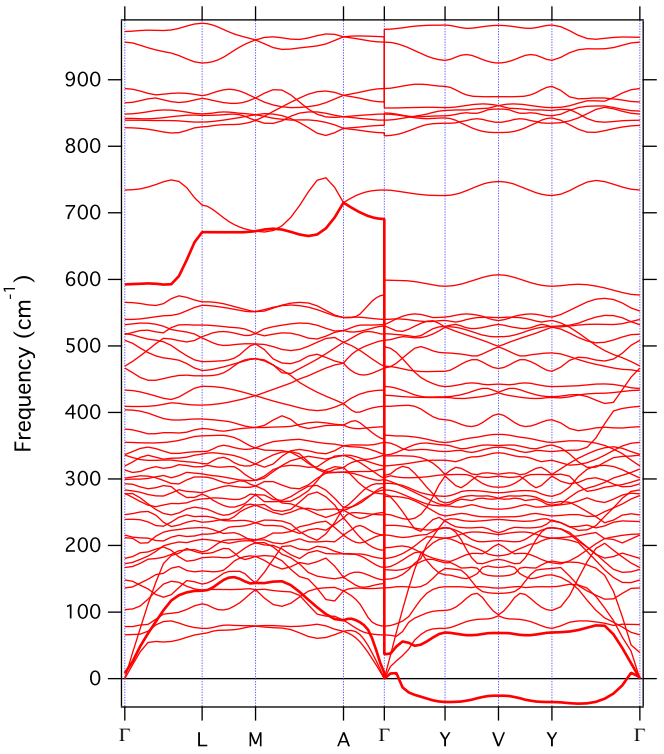

FIG. 12. Phonon dispersion curves in the $C2/c$ symmetry, calculated using the PBEsol XC functional.

caused by the unstable B_u phonons, is going to soften these acoustic branches and other low-lying modes with dominant Ca motion. Such a coupled mode softening is likely to contribute to the diffuse scattering at elevated temperatures.

We recall here that the PBEsol XC functional, while yielding relatively accurate lattice parameters, did not reproduce the distortion of the titanite structure in the ordered $P2_1/c$ phase. Figure 12 shows the parent phase phonon dispersion obtained with the PBEsol XC functional. Two details are immediately obvious: the maximum LO-TO splitting at the center of the diagram is still extremely large, but smaller than with either PBE or RPBE and the TO side is stable at 36 cm^{-1}. The other obvious difference to Figs. 5 and 6 is that an imaginary phonon branch exists too, but that it is much closer to zero frequency than the imaginary branches calculated with the PBE and RPBE XC functionals. The imaginary branch starts as a stable TA phonon at Γ, but it drops to imaginary frequencies while approaching Y, avoiding the crossing with the lowest-lying TO-phonon branch (the unstable mode in the PBE and RPBE calculations). There is strong overlap of the eigenvectors of both modes in the wave-vector region close to Γ, confirming the strong coupling that gives rise to the avoided crossing of the branches. Contrary to the case of the other GGA functionals, PBEsol predicts some frequency dispersion along the path Γ-Y-V-Y-Γ, with slight frequency increase close to V, but the minimum at Y is not very well defined either. The imaginary frequency parts of this phonon branch represent similar Ti motion as described in Figs. 8(b)–8(d). Only the potentially ferroelectric displacement shown in Fig. 8(a) is now replaced by a stable optical phonon. The first stable frequency at the Y point corresponds to a phonon mode with very similar motion to that shown in Fig. 11(b) and similar frequency to the PBE result (69.3 compared to 78.1 cm^{-1}).

The frequency modulus of the unstable TO phonon at the Y point correlates with the amount of Ti displacement obtained in the $P2_1/c$ distorted phase for each of the XC functionals. This indicates that the PBE functional provides the best compromise between an accurate volume prediction on one hand and an accurate prediction of the structural distortions involved in the $C2/c$ to $P2_1/c$ phase transition on the other hand. Using the PBEsol functional, the distortion and the associated energy difference in particular is underestimated, which might be due to the general incongruence between the lattice parameters and the total energies to be expected from GGA functionals [35]. Nevertheless, the results obtained with PBEsol are of interest because of the observed strong coupling between the (lowest-frequency) transverse optical phonon and the transverse acoustic phonon, when the former approaches the frequency of the latter.

IV. CONCLUSIONS

The antipolar distortion of Ti atoms in the low-temperature titanite structure is strongly volume dependent. While the PBE functional correctly reproduces the distorted structure, the PBEsol functional that yields smaller lattice parameters for the fully relaxed structure tends to strongly underestimate the distortion. The RPBE XC functional overestimates the distortion, which correlates with the strongly overestimated lattice volume. Experimentally, the distorted $P2_1/c$ structure is known to transform to the undistorted $C2/c$ structure at relatively low pressures of 3.5 GPa and a volume compression of about 3% (358.34 Å^3, Ref. [21]) relative to a zero-pressure volume of 370 Å^3. Such a volume compression is well within the range of volume changes induced by variation of the XC functional. For the aristotype symmetry $C2/c$ all three GGA functionals predict an unstable phonon branch with wave vectors normal to the [001] direction, corresponding to a B_u mode at the BZ center. The average frequency and dispersion of this branch again depend on the volume as calculated with the different functionals.

The occurrence of an unstable phonon branch in the $C2/c$ titanite structure indicates that the transition to the ordered $P2_1/c$ structure is unlikely to proceed via freezing of a single optical BZ boundary phonon mode, as would be expected in a strictly displacive-type phase transition. Instead, a continuous spectrum of phonon modes, located in the zero-level BZ layer normal to [001], is destabilized on lowering the temperature. The local Ti displacements that arise from the instability develop in a correlated fashion along individual octahedral chains, while correlations with the adjacent displacement chains vary with the position along the phonon branch. The unit that is unstable against displacement is a chain of Ti atoms, as opposed to a single atom, a behavior that has been described in Ref. [5] for $KNbO_3$ perovskite. While there are three equivalent chain directions in the cubic perovskites, there is only one chain direction, [001], in titanite. Correlations in lateral direction to the chains will be weak and the polar distortion that arises at the Γ point can even become equally unstable as the antipolar distortion arising at the Y point. This

picture is in agreement with the observation of layers of diffuse scattering normal to the [001] chain direction that can persist up to 825 K in titanite. It is expected that altering the lateral coupling strength of the chains by application of structural stress can be used to control the pattern of the two-dimensional displacement ordering, allowing for example a polar distortion of the titanite structure with potentially ferroelectric properties. This can either be achieved by dilatation of the interchain distances by modification of the *A* and *X* cation radius, or by growth of titanite layers oriented normal to [001] on suitable substrates.

ACKNOWLEDGMENTS

The authors acknowledge the North-German Supercomputing Alliance (HLRN) for providing HPC resources that have contributed to the results reported in this paper. Help with compiling CASTEP was kindly provided by C. Tuma. The authors are grateful to U. Bismayer for providing the pristine titanite crystal used to demonstrate the diffuse scattering in Fig. 2. Funding of M.F. was provided by the Central Research Development Fund (CRDF) of the University of Bremen (Funding line 04–Independent Projects for Post-Docs).

[1] I. B. Bersuker, Phys. Rev. Lett. **108**, 137202 (2012).
[2] R. E. Cohen, Nature (London) **358**, 136 (1992).
[3] I. B. Bersuker, Chem. Rev. **113**, 1351 (2013).
[4] R. Comès, M. Lambert, and A. Guinier, Acta Crystallogr. Sect. A **26**, 244 (1970).
[5] R. Yu and H. Krakauer, Phys. Rev. Lett. **74**, 4067 (1995).
[6] H. Krakauer, R. Yu, C. Wang, K. M. Rabe, and U. V. Waghmare, J. Phys.: Condens. Matter **11**, 3779 (1999).
[7] M. S. Senn, D. A. Keen, T. C. A. Lucas, J. A. Hriljac, and A. L. Goodwin, Phys. Rev. Lett. **116**, 207602 (2016).
[8] R. Comes, M. Lambert, and A. Guinier, Solid State Commun. **6**, 715 (1968).
[9] J. Kimura, H. Taniguchi, T. Iijima, T. Shimizu, S. Yasui, M. Itoh, and H. Funakubo, Appl. Phys. Lett. **108**, 062902 (2016).
[10] M. Taylor and G. E. Brown, Am. Mineral. **61**, 435 (1976).
[11] S. Ghose, Y. Ito, and D. M. Hatch, Phys. Chem. Miner. **17**, 591 (1991).
[12] M. Zhang, E. Salje, U. Bismayer, H. Unruh, B. Wruck, and C. Schmidt, Phys. Chem. Miner. **22**, 41 (1995).
[13] C. Van Heurck, G. Van Tendeloo, S. Ghose, and S. Amelinckx, Phys. Chem. Miner. **17**, 604 (1991).
[14] T. Malcherek, C. Paulmann, M. C. Domeneghetti, and U. Bismayer, J. Appl. Crystallogr. **34**, 108 (2001).
[15] S. Kek, M. Aroyo, U. Bismayer, C. Schmidt, K. Eichhorn, and H. G. Krane, Z. Kristallogr. **212**, 9 (1997).
[16] T. Malcherek, Mineral. Mag. **65**, 709 (2001).
[17] E. Salje, C. Schmidt, and U. Bismayer, Phys. Chem. Miner. **19**, 502 (1993).
[18] M. Zhang, E. Salje, and U. Bismayer, Am. Mineral. **82**, 30 (1997).
[19] U. Bismayer, W. Schmahl, C. Schmidt, and L. Groat, Phys. Chem. Miner. **19**, 260 (1992).
[20] M. Kunz, T. Arlt, and J. Stolz, Am. Mineral. **85**, 1465 (2000).
[21] R. J. Angel, M. Kunz, R. Miletich, A. B. Woodland, M. Koch, and D. Xirouchakis, Phase Transitions **68**, 533 (1999).
[22] R. Ellemann-Olesen and T. Malcherek, Am. Mineral. **90**, 1325 (2005).
[23] T. Malcherek, Acta Crystallogr. Sect. B **63**, 545 (2007).
[24] M. Kunz, D. Xirouchakis, Y. Wang, J. B. Parise, and D. H. Lindsley, Schweiz. Mineral. Petrogr. Mitteil. **77**, 1 (1997).
[25] R. Ellemann-Olesen and T. Malcherek, Am. Mineral. **90**, 687 (2005).
[26] T. Malcherek, J. Appl. Crystallogr. **44**, 585 (2011).
[27] X. Gonze, Phys. Rev. B **55**, 10337 (1997).
[28] X. Gonze and C. Lee, Phys. Rev. B **55**, 10355 (1997).
[29] S. J. Clark, M. D. Segall, C. J. Pickard, P. J. Hasnip, M. I. J. Probert, K. Refson, and M. C. Payne, Z. Kristallogr. **220**, 567 (2005).
[30] K. Refson, P. R. Tulip, and S. J. Clark, Phys. Rev. B **73**, 155114 (2006).
[31] J. W. Bennett, Phys. Procedia **34**, 14 (2012).
[32] A. M. Rappe, K. M. Rabe, E. Kaxiras, and J. D. Joannopoulos, Phys. Rev. B **41**, 1227 (1990).
[33] J. P. Perdew, K. Burke, and M. Ernzerhof, Phys. Rev. Lett. **77**, 3865 (1996).
[34] B. Hammer, L. B. Hansen, and J. K. Nørskov, Phys. Rev. B **59**, 7413 (1999).
[35] J. P. Perdew, A. Ruzsinszky, G. I. Csonka, O. A. Vydrov, G. E. Scuseria, L. A. Constantin, X. Zhou, and K. Burke, Phys. Rev. Lett. **100**, 136406 (2008).
[36] P. Haas, F. Tran, P. Blaha, and K. Schwarz, Phys. Rev. B **83**, 205117 (2011).
[37] G. I. Csonka, J. P. Perdew, A. Ruzsinszky, P. H. T. Philipsen, S. Lebègue, J. Paier, O. A. Vydrov, and J. G. Ángyán, Phys. Rev. B **79**, 155107 (2009).
[38] T. S. Bjørheim, E. A. Kotomin, and J. Maier, J. Mater. Chem. A **3**, 7639 (2015).
[39] M. J. Gutmann, K. Refson, M. v Zimmermann, I. P. Swainson, A. Dabkowski, and H. Dabkowska, J. Phys.: Condens. Matter **25**, 315402 (2013).
[40] D. Orobengoa, C. Capillas, M. I. Aroyo, and J. M. Perez-Mato, J. Appl. Crystallogr. **42**, 820 (2009).
[41] T. Proffen and R. B. Neder, J. Appl. Crystallogr. **32**, 838 (1999).
[42] M. I. Aroyo, D. Orobengoa, G. de la Flor, E. S. Tasci, J. M. Perez-Mato, and H. Wondratschek, Acta Crystallogr. Sect. A **70**, 126 (2014).
[43] W. Zhong, R. D. King-Smith, and D. Vanderbilt, Phys. Rev. Lett. **72**, 3618 (1994).
[44] T. Beirau, B. Mihailova, G. Matveeva, U. Kolb, T. Malcherek, L. A. Groat, and U. Bismayer, Am. Mineral. **97**, 1354 (2012).
[45] J. Hlinka, T. Ostapchuk, D. Nuzhnyy, J. Petzelt, P. Kuzel, C. Kadlec, P. Vanek, I. Ponomareva, and L. Bellaiche, Phys. Rev. Lett. **101**, 167402 (2008).
[46] M. Posternak, R. Resta, and A. Baldereschi, Phys. Rev. B **50**, 8911 (1994).
[47] I. Tanaka, T. Obuchi, and H. Kojima, J. Cryst. Growth **87**, 169 (1988).